XI International Conference on Computational Methods for Coupled Problems in Science and Engineering
COUPLED PROBLEMS 2025
A. Larese, S. Perotto and G. Rozza (Eds)

DEVELOPMENT AND PRELIMINARY ANALYSIS OF A MULTIPHYSICS NUMERICAL PLATFORM FOR PREDICTING THERMAL BEHAVIOR IN AUTOMOTIVE LITHIUM BATTERIES

D. FEDELI[*], M. LAGNONI[*], C. SCARPELLI[†], F. G. QUILICI[†], A. BERTEI[*], G. LUTZEMBERGER[†], M. V. SALVETTI[*], A. MARIOTTI[*]

[*]Dipartimento di Ingegneria Civile e Industriale, Università di Pisa, Largo Lucio Lazzarino 2, Pisa, Italy
[†]Dipartimento di Ingegneria dell'Energia, dei Sistemi, del Territorio e delle Costruzioni, Università di Pisa, Largo Lucio Lazzarino 2, Pisa, Italy

Key words: Multiphysics Platform, Computational Fluid Dynamics (CFD), Conjugate Heat Transfer (CHT), Lithium Batteries, Experimental Validation

Abstract. The lithium-ion battery is essential for advancing the next generation of electric transportation. A key factor in maximizing the efficiency and safety of these batteries is optimizing their thermal management system. To achieve this, we have developed a multiphysics numerical platform for the battery cell to study its thermal behavior throughout its operating cycle. This approach combines Computational Fluid Dynamics (CFD) simulations to evaluate the external cooling system, a zero-dimensional electro-thermal model for internal heat generation, and Conjugate Heat Transfer (CHT) to capture the thermal coupling between the cell core and its external surface. The aim of this study is to reproduce how a prismatic lithium-ion cell heats up during a 1C charging cycle and to investigate its thermal response under different air-cooling conditions, namely natural and forced convection. The proposed methodology was validated through a dedicated wind-tunnel experiment, in which the same prismatic cell was subjected to controlled charge-discharge cycles using a battery cycler while varying the external airflow velocity to reproduce the different cooling regimes. The preliminary results obtained with this platform have been validated against wind tunnel tests, both with and without wind. The numerical results accurately replicate the temperature gradients within the battery for the 1C charging cycle, with differences from experimental measurements typically within a few percentage points.

1 Introduction

The ongoing energy transition is driving a profound transformation of industrial processes, especially in the automotive sector. Battery electric vehicles (BEVs) have emerged as one of the pillars of sustainable mobility, with the battery pack representing both the energy reservoir and one of the most critical components in terms of safety, performance, and lifetime [1].

Thermal management plays a fundamental role in lithium-ion battery operation. These cells must operate within a narrow temperature range to maintain electrochemical performance, ensure efficiency, and avoid accelerated degradation. Uncontrolled temperature rise can trigger safety issues such as thermal runaway [2]. Heat generation originates from two main sources:

irreversible Joule heating due to internal resistances, and reversible contributions related to entropic effects [3]. During charge and discharge cycles, these phenomena combine to produce heat that must be dissipated effectively to preserve cell integrity.

Accurate modeling of both internal heat generation and external heat dissipation is essential for designing reliable Battery Thermal Management Systems (BTMS). Computational fluid dynamics (CFD) provides a powerful tool to resolve coupled conduction and convection phenomena, with conjugate heat transfer (CHT) enabling physically consistent representation under realistic operating conditions.

Several studies have demonstrated the effectiveness of detailed CFD models at the single-cell level. Three-dimensional predictions can reproduce experimental temperature fields within a few degrees under natural convection [5], while validated electro-thermal CFD models for prismatic cells under forced convection confirm the importance of boundary condition fidelity.. Air cooling remains attractive for its simplicity and scalability, despite limitations in temperature uniformity [6]. Complementary CHT investigations [7] underline the importance of properly defining thermal boundary conditions and material interfaces for quantitative model validation.

In this work, we develop a numerical platform capable of predicting the thermal behaviour of a prismatic $LiFePO_4$ cell representative of automotive applications. The platform couples a zero-dimensional electro-thermal model of heat generation with three-dimensional CHT simulations in a CFD environment, enabling physically consistent prediction of temperature distribution under realistic operating conditions. The predictions are validated against dedicated wind tunnel experiments with surface temperature measurements under different cooling conditions (natural and forced convection). This single-cell validation establishes a foundation for future module- and pack-level simulations.

2 Development of the multiphysics numerical platform

We describe herein the main features of the development of a multiphysics numerical platform aimed at computing the coupling between the electro-thermal behaviour inside a $LiFePO_4$ cell, the heat transport and the battery cooling. The platform has been conceived to reproduce realistic operating conditions under both passive and active air cooling, with the long-term perspective of extending the methodology to larger assemblies of cells, such as modules or packs. In order to achieve this goal, the methodology is divided into three interconnected components: (i) geometrical modelling of the battery cell and the conjugate heat transfer, (ii) implementation of the electro-thermal heat generation model within the CFD solver, (iii) flow conditioning and a quasi-steady numerical strategy for evaluating cooling solutions under appropriate boundary conditions and meshing. Each component is described in detail in the following subsections. A scheme of the three components can be observed in Figure 2.1

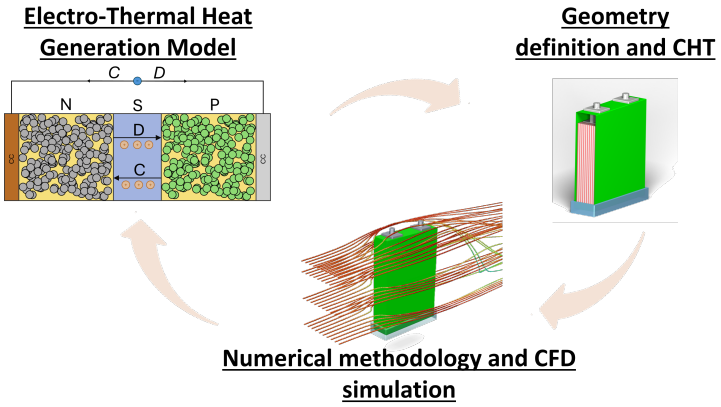

Figure 2.1: Conceptual scheme of the numerical platform

2.1 Geometry definition and conjugate heat transfer

A detailed three-dimensional model of the $LiFePO_4$ prismatic cell was constructed in order to replicate faithfully the dimensions and main geometrical features of the real specimen. All external dimensions of the casing and cell geometry are preserved. Internally, the battery is constituted by a large number of alternating layers of positive electrode, separator, and negative electrode. The real device comprises tens of such stacked layers, which makes a fully resolved layer-by-layer model computationally prohibitive.

To reduce complexity while retaining physical representativeness, the internal structure was homogenised into alternating blocks of active and inactive material. The properties of these homogenised blocks were assigned consistently with the electro-thermal model (see Section 2.2), so that the effective thermophysical behaviour corresponds to that of the real multi-layered cell. The distinction between active and inactive volumes is essential: only the active regions are allowed to generate heat, in accordance with the physical heat production mechanism. Unlike other approaches that exploit symmetry, the entire cell was simulated in order to preserve the correct flow and thermal boundary conditions.

As mentioned above the cell that will be tested is a LFPO4 60Ah prismatic with excellent performances regarding power delivery, especially in the automotive field. The cell was placed in the wind tunnel using a custom-designed 3D-printed support, specifically developed to ensure the stiffness required for the experimental tests. The electrical connection was made with cables carefully arranged so as not to affect the aerodynamic flow, connected to equipment capable of controlling charging and discharging cycles, with voltage and current measurements acquired through a LabVIEW-managed system.

2.2 Electro-Thermal Heat Generation Model

The thermal source term is derived from an electro-thermal model based on Bernardi *et al.* [4], providing instantaneous heat generation as a function of cell voltage, state of charge (SOC), and temperature. We adopt the implementation described in Lagnoni *et al.* [8], which combines an equivalent electrical circuit (EEC) with a lumped two-node thermal network for voltage and temperature evolution under realistic conditions.

The electrical sub-model reproduces cell voltage through open-circuit potential, series ohmic

resistance, and a parallel R_1C_1 branch capturing electrochemical dynamics. All parameters depend on SOC and temperature to represent nonlinear charge–discharge behaviour. The thermal model includes core heat capacity and two resistances describing conduction through the cell body and convection to ambient air. Heat generation is computed from irreversible Joule losses, which dominate in $LiFePO_4$ cells. Parameters were calibrated on a 60 Ah prismatic cell using multi-step electrical and thermal tests, yielding mean voltage error below 1% and surface temperature deviation under 1 K. Since the model outputs are tabulated at discrete operating points, polynomial interpolation provides a smooth function for CFD coupling. At each CFD time step, an internal routine reads the local temperature of each computational cell, determines the corresponding time instant to infer SOC, evaluates the interpolated function, and computes the local volumetric heat generation rate q''' (W/m^3), which is applied as a source term in the energy equation. This procedure captures spatial and temporal heat distribution within the active material. The charging process operates at 1C rate, defined as

$$\text{C-rate} = \frac{I}{C_{\text{nom}}} \tag{1}$$

where I is the applied current (A) and C_{nom} the nominal capacity (Ah).

2.3 Numerical methodology and CFD simulation set-up

The CFD procedure is based on the incompressible Reynolds-Averaged Navier-Stokes (RANS) equations governing air flow around the battery:

$$\nabla \cdot \mathbf{u} = 0, \tag{2}$$

$$\rho \left(\frac{\partial \mathbf{u}}{\partial t} + \mathbf{u} \cdot \nabla \mathbf{u} \right) = -\nabla p + \nabla \cdot \left[\mu \left(\nabla \mathbf{u} + (\nabla \mathbf{u})^T \right) - \rho \overline{u_i' u_j'} \right], \tag{3}$$

$$\rho c_p \left(\frac{\partial T}{\partial t} + \mathbf{u} \cdot \nabla T \right) = \nabla \cdot (k \nabla T) + S_T, \tag{4}$$

where $\mathbf{u}$ and p denote the time-averaged velocity and pressure fields, respectively, T is the temperature field, ρ is the air density, μ is its dynamic viscosity, c_p is the specific heat at constant pressure, k is the thermal conductivity, and S_T is an energy source term. $\overline{u_i' u_j'}$ represents the Reynolds stress tensor. The equations are closed using the Shear Stress Transport (SST) k-ω turbulence model, which provides reliable near-wall flow predictions and accurate resolution of adverse pressure gradients.

At the inlet of the computational domain, a boundary condition of constant velocity in the x-component ($u_x = U_{inlet}$, $u_y = 0$, $u_z = 0$) and a constant temperature of $T = 23°C$ has been assigned.

Discretization and solution strategy: The governing equations are discretized using a finite-volume method on unstructured grids with second-order accuracy. Convective terms use a second-order upwind scheme, while diffusive terms are treated implicitly. Pressure and momentum equations are solved through a pressure-based coupled algorithm that simultaneously handles continuity and momentum, improving robustness and convergence and ensuring consistency by directly discretizing pressure-gradient terms within the momentum equations.

Temporal strategy: The simulation employs a two-step procedure separating aerodynamic convergence from thermal transients. First, a fluid-only computation with no heat source and fine temporal resolution ($\Delta t_{\text{flow}} = 10^{-4}$ s) runs until the aerodynamic field becomes quasi-steady. Then, the electro-thermal cycle begins, with heat generation updated every $\Delta t_{\text{thermal}} = 10$ s, consistent with the slower thermal evolution characteristic of 1C charging.

Boundary conditions: The analysis considers natural convection ($v = 0$ m/s) and forced convection at 10 m/s and 20 m/s. The outlet is prescribed as a pressure boundary at ambient pressure, all other external boundaries are adiabatic, and no-slip conditions apply on battery surfaces.

Mesh generation: The computational grid is composed mainly of trimmed hexahedral cells to balance accuracy and efficiency. Prism layers near solid walls ensure proper boundary-layer resolution and reliable convective heat transfer prediction. Grid-independence verification demonstrated insensitivity to further refinement, and both temporal and iterative convergence were confirmed.

Overall, the methodology provides a consistent framework in which electro-thermal processes inside the cell are coupled to external convection. The wake-control plate and the quasi-steady strategy allow the single-cell setup to represent module-level cooling behaviour, forming a solid basis for future multi-cell extensions.

2.3.1 Wake Suppression and Quasi-steady Numerical Strategy

When placed in cross-flow with its smaller side perpendicular to the incoming air, the prismatic cell behaves as a bluff body. As such, it is subject to vortex shedding, which produces a strongly unsteady wake. This behaviour, while physically correct, does not represent the intended cooling environment of a real battery pack, where neighbouring cells and pack structure suppress such large oscillations and stabilise the flow.

To approximate such conditions in a single-cell simulation, a flat plate was designed and positioned at the base of the cell, closing the near wake and suppressing vortex shedding. This design, first conceived in CFD, was also replicated in the experimental campaign to ensure consistency between numerical and physical setups. The presence of the plate yields a quasi-steady velocity field around the battery, more representative of a real module environment.

3 Experimental set-up

The experimental setup adopted in this work was inspired by the procedure presented by Barbieri *et al.* [9], who proposed and validated an electro-thermal characterization method for large prismatic $LiFePO_4$ cells. Given the similarity between their test cell and the one analyzed in the present study, the same approach was employed for the temperature acquisition and calibration phases. The experimental setup includes a battery cycler with a 60 V-250 A Ametek SPS60x250-K02D charger [10] and a 60 V-500 A Zentro-Elektrik EL6000 discharger [11], remotely controlled through LabVIEW software. Voltage and current are measured by a National Instruments DAQ 9219, which has a 100 ms acquisition rate. At the same time, the temperature distribution is monitored using 30 K-type probes. Experimental investigations were carried out in the wind tunnel of the Department of Civil and Industrial Engineering at the University of Pisa. This is a subsonic close jet tunnel with an open test section. The test section is circular with a diameter of 1.10 m and a length of 1.42 m. The velocity range is between 5 and 35 m/s

and the turbulence intensity of the free stream is equal to 0.9%. The engine is located outside the duct and only the propeller connected to the motor shaft is present inside. Aerodynamic profiles are located at the corners to straighten the flow. The wind tunnel of the University of Pisa has been widely used and validated for investigations on bluff-body flows in the last decades and additional details on the facility can be found, e.g., in [13, 14].

The reference system used in the wind tunnel is represented in Figure 3.1a: the x-axis is directed as the freestream velocity, the y-axis is perpendicular to the floor and directed upward while the z-axis is the other element in the right-handed tern.

The temperature measurements were carried out through one PT100 thermoresistance and 30 type K thermocouples, which were fixed to the external surface of the battery at significant points, so as to create a matrix of measuring points on the surface and observe the temperature distribution in all dimensions. The charging and discharging cycles were controlled using the previously desciribed battery cycler, managed entirely via the LabVIEW platform.

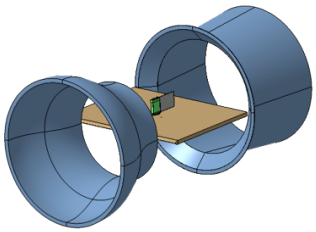

(a) Scheme of the test section with a single cell mounted for the experiment.

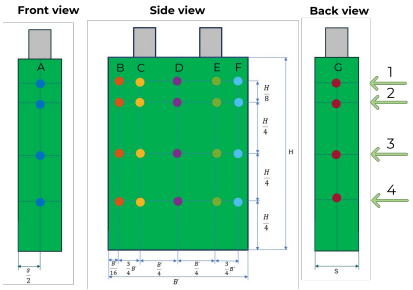

(b) Thermocouples map.

Figure 3.1: Experimental setup: (a) schematic of the wind tunnel test section; (b) thermocouple distribution on the cell surface.

At the beginning of the analysis, it is useful to clarify the location and naming convention adopted for the monitoring points on the battery surface. Figure 3.1b shows the schematic representation of the measurement layout, where several virtual probes are placed at specific positions corresponding to those where type-K thermocouples were installed during the experimental campaign. In this scheme, each *slice* corresponds to a horizontal plane containing seven probes positioned at the same height along the cell. The different slices are identified by distinct symbols, which indicate the vertical level of measurement, while the probe colours denote their relative position on the cell surface (front, rear, and lateral sides). It is important to note that thermocouples were placed only on one of the two lateral faces, as preliminary tests demonstrated a symmetrical temperature distribution. This convention is consistently adopted throughout the following sections for both CFD and experimental data presentation, ensuring direct correspondence between numerical and experimental results.

4 Preliminary results

The results of the experimental campain and thermo-fluid dynamics simulations are presented in this section, focusing on the wall temperature distribution under different cooling conditions of the $LiFePO_4$ cell during the charging cycle. The simulation outputs are compared with the experimental data for validation purposes.

4.1 Experimental results for natural convection

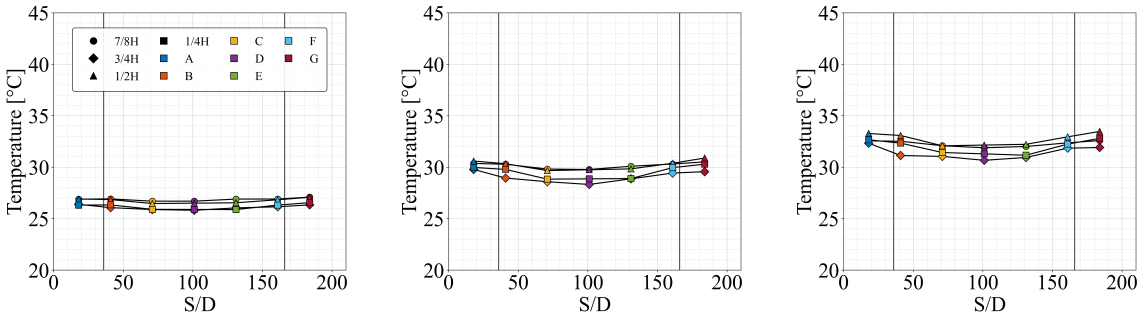

(a) $t = 1200$ s (b) $t = 2400$ s (c) $t = 3600$ s

Figure 4.1: 1C charging cycle, $v = 0$ m/s – Temperature distribution during the cycle.

Figure 4.1 shows three representative snapshots of the wall temperature distribution at $t = 1200$ s, $t = 2400$ s, and $t = 3600$ s, when there is no active cooling. It is possible to observe how the temperature increases monotonically and rather uniformly across the entire cell surface, with no appreciable differences between the front, rear, and lateral faces. This indicates that, under natural convection, heat transfer within the solid domain is dominant and temperature gradients are negligible. Under natural convection, the temperature rise is nearly uniform across all probe positions. The absence of significant airflow leads to a homogeneous temperature field within the cell, with only small deviations (below 1 K) between different measurement points. The overall temperature increase is governed mainly by internal heat conduction and the weak buoyancy-driven motion of the surrounding air.

4.2 Experimental results for forced convection at 10 m/s

To evaluate the influence of forced convection, the same 1C charging cycle was simulated under an imposed air velocity of $10\ \mathrm{m/s}$. Figure 4.2 shows three representative snapshots of the wall temperature distribution at $t = 1200$ s, $t = 2400$ s, and $t = 3600$ s.

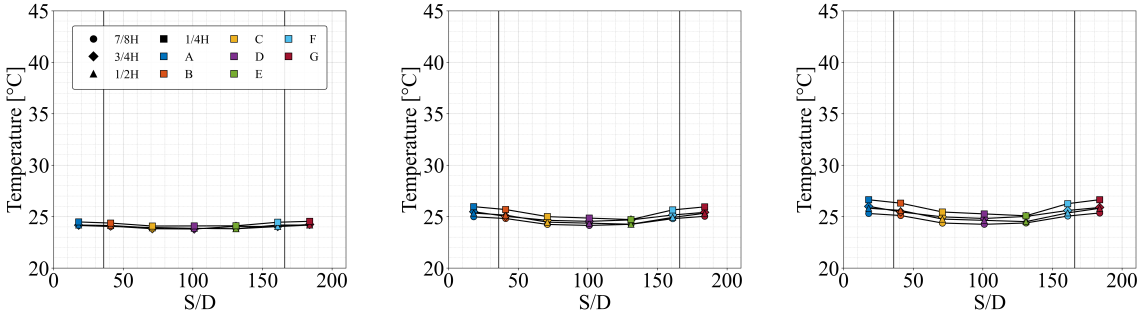

(a) $t = 1200$ s (b) $t = 2400$ s (c) $t = 3600$ s

Figure 4.2: 1C charging cycle, $v = 10$ m/s – Temperature distribution during the cycle.

Compared with the natural convection case, the introduction of a forced air stream at $10\ \mathrm{m/s}$ results in an overall reduction of the surface temperature on all faces of the cell. The airflow

enhances heat removal, limiting the maximum temperature rise during the cycle. However, the temperature field becomes less uniform: horizontal gradients, oriented along the main flow direction, are clearly visible. The windward face, directly impacted by the air stream, remains consistently cooler, whereas the leeward side exhibits slightly higher temperatures due to reduced convective exchange in the wake region. Vertical gradients are also more evident in this configuration. The bottom portion of the cell, where the boundary layer is still developing and airflow velocities are lower, tends to remain warmer, while the upper region shows a modestly lower temperature, consistent with buoyancy effects and enhanced mixing at higher elevations. These observations highlight how even a moderate airflow is sufficient to alter the thermal symmetry observed under natural convection.

4.3 Experimental results for forced convection at 20 m/s

A further increase in the external airflow velocity to $20\ \mathrm{m/s}$ intensifies these effects. Figure 4.3 presents the corresponding wall-temperature distributions at $t = 1200$ s, $t = 2400$ s, and $t = 3600$ s.

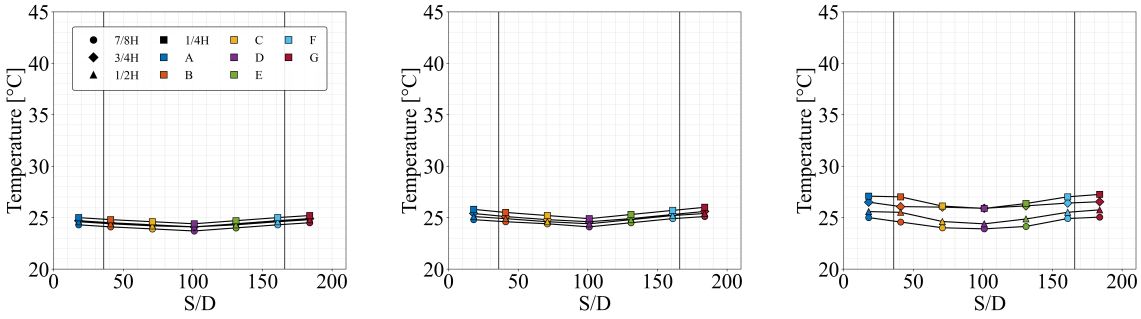

(a) $t = 1200$ s (b) $t = 2400$ s (c) $t = 3600$ s

Figure 4.3: 1C charging cycle, $v = 20$ m/s – Temperature distribution during the cycle.

At the higher velocity, convective heat transfer becomes dominant, leading to a significant reduction of the maximum surface temperature compared to the 10 m/s case. The horizontal temperature gradients are more pronounced, with a clear distinction between the cooler upstream region and the warmer downstream area, where the air has already absorbed heat from the cell surface. The vertical gradients are also intensified: the lower part of the battery remains the warmest zone, while the upper region, exposed to a stronger and more turbulent flow, exhibits lower temperatures. Overall, the results confirm that increasing the airflow velocity enhances the global cooling effectiveness but simultaneously increases the spatial non-uniformity of the surface temperature. These features are consistent with the expected behaviour of a bluff body subjected to forced convection and will be quantitatively compared with experimental measurements in the following section.

4.4 CFD results for natural convection

As shown in Figure 4.4, the CFD results under natural convection conditions demonstrate that the proposed methodology successfully reproduces the gradual heating of the battery throughout the charging cycle. The temperature field remains almost uniform across the surface, and

the heat distribution is mainly governed by internal conduction.

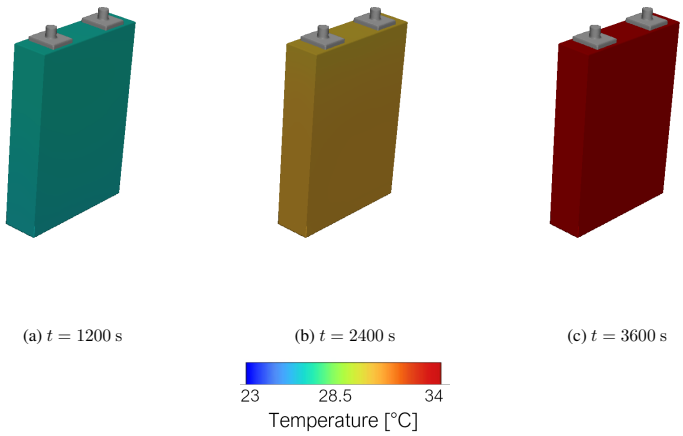

Figure 4.4: 1C charging cycle, $v = 0$ m/s – Contour of wall temperature during the cycle.

4.5 CFD results for forced convection at 10 m/s

The numerical results for the 10 m/s case, illustrated in Figure 4.5, confirm that the cell undergoes a progressive and controlled temperature increase during the 1C charging cycle. Toward the end of the cycle, a distinct temperature rise is detected, accompanied by the emergence of horizontal and vertical gradients across the cell surface.

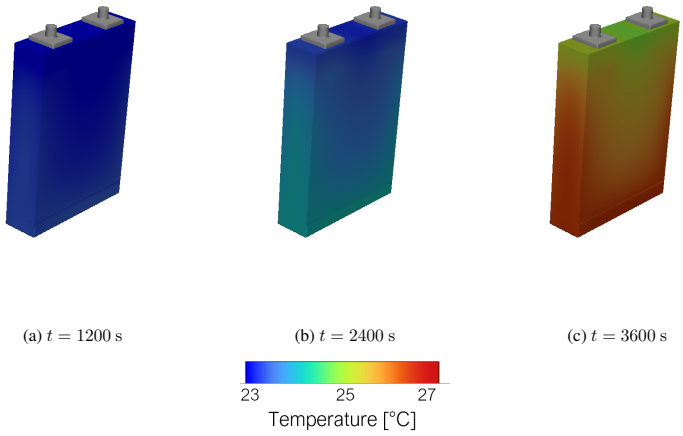

Figure 4.5: 1C charging cycle, $v = 10$ m/s – Contour of wall temperature during the cycle.

4.6 CFD results for forced convection at 20 m/s

Figure 4.6 presents the CFD results for the highest airflow condition, showing once again a gradual heating of the cell over time, with a sharp temperature spike near the end of the cycle. In this configuration, both horizontal and vertical temperature gradients become more pronounced, evidencing the combined influence of strong forced convection and localized flow separation.

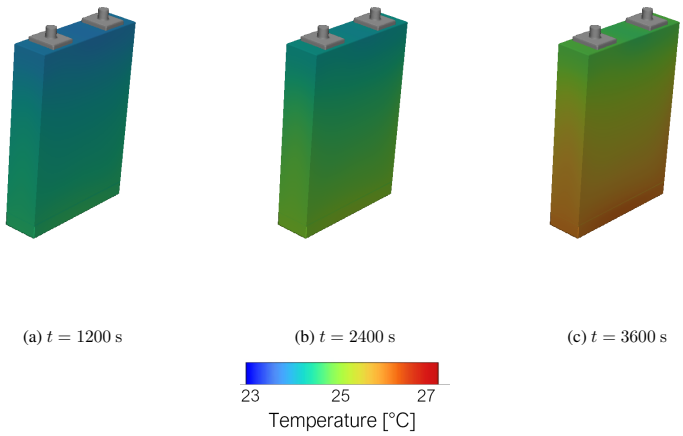

Figure 4.6: 1C charging cycle, $v = 20$ m/s – Contour of wall temperature during the cycle.

4.7 Experimental validation with numerical simulations

To assess the reliability of the developed numerical platform, the CFD results were compared with experimental data obtained from the wind tunnel campaign. The comparison was carried out by matching the temperature evolution at the same positions where the thermocouples were installed.

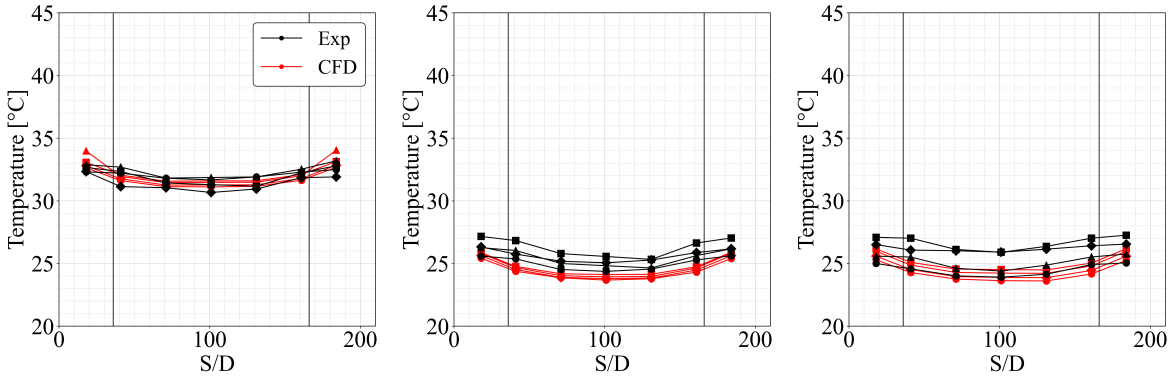

(a) $v = 0$ m/s (b) $v = 10$ m/s (c) $v = 20$ m/s

Figure 4.7: Comparison between CFD and experimental results

As shown in Figure 4.7, the numerical predictions reproduce the experimental temperature trends with good accuracy across all operating conditions. Both the transient behaviour and the final temperature levels agree well with measurements, with deviations generally within the thermocouple uncertainty (± 1.5 K). A slight overprediction during the early charging phase is attributed to local variations in the convective heat transfer coefficient not captured by the steady–state flow approximation. A quantitative comparison was carried out for the three airflow conditions at 1C, evaluating percentage deviations at the four thermocouple planes (1/4H, 1/2H, 3/4H, 7/8H). Overall agreement is very good, with discrepancies typically below 2% for natural and moderate forced convection, and moderately higher deviations at the highest velocity.

Under natural convection ($v = 0\ \mathrm{m/s}$), Figure 4.7a, deviations remain consistently low across all planes, with maximum values around 2%. The absence of spatial trends confirms the model's ability to reproduce the nearly uniform temperature field observed when conduction dominates.

At $v = 10\ \mathrm{m/s}$, Figure 4.7b, percentage errors remain below 1.5% for all slices, typically in the 0.5–1.2% range. Slightly higher deviations appear near 7/8H due to increased sensitivity to turbulence modeling and mesh resolution. The systematic underestimation of less than 1% indicates stable model behaviour and consistent prediction of conjugate heat transfer.

At $v = 20\ \mathrm{m/s}$, Figure 4.7c, local discrepancies increase, particularly at 3/4H and 1/4H, reaching up to 8%. The higher Reynolds number amplifies wake dynamics and turbulence fluctuations, affecting heat transfer coefficients. The model mildly underpredicts cooling efficiency, though the overall distribution of thermal gradients remains correctly captured. The 7/8H and 1/2H regions maintain deviations within 2–3%. The observed errors lie within expected uncertainty ranges of thermal measurements and turbulence modeling.

5 Conclusions

A multiphysics numerical platform was developed to couple a zero–dimensional electro–thermal heat generation model with three–dimensional CFD simulations of conjugate heat transfer in a prismatic $LiFePO_4$ cell. The approach integrates the model of Lagnoni *et al.* [8] through a user–defined function that updates the volumetric heat source based on local temperature and state of charge.

The numerical results demonstrate accurate prediction of both transient evolution and spatial temperature distribution. The platform offers a robust basis for analysing coupled electro–thermal and fluid–dynamic phenomena in lithium–ion cells and can be extended to multi–cell modules, where cell–to–cell interactions and cooling strategies become critical. Future work will refine the coupling procedure, broaden the validation dataset, and include additional effects such as radiation and contact resistances to improve predictive capability.

REFERENCES

[1] Abbas, S. A.; Khan, A.; Shah, M. A.; et al. "A Review of Improvements on Electric Vehicle Battery". *Processes*, (2024), 12, 5, 789.

[2] Ceraolo, M., Lutzemberger, G., Poli, D., Scarpelli, C. "Luenberger-based State-Of-Charge Evaluation and Experimental Validation with Lithium Cells." *Journal of Energy Storage*, (2020), 30, 101534.

[3] Lagnoni, M.; Scarpelli, C.; Lutzemberger, G.; Bertei, A. "Critical Comparison of Equivalent Circuit and Physics-Based Models for Lithium-Ion Batteries: A Graphite/Lithium-Iron-Phosphate Case Study". *Journal of Energy Storage*, (2024), 94, 112326.

[4] Bernardi, D.; Pawlikowski, E.; Newman, J. "A General Energy Balance for Battery Systems". *Journal of The Electrochemical Society*, (1985), 132, 5, 5–12.

[5] Gümüşsu, E., Karadeniz, H., and Kılıç, F. "CFD simulation and experimental validation of the thermal behavior of a single lithium-ion battery cell under natural convection". *Applied Thermal Engineering*, (2017), 121, 784–795.

[6] Sheng, L., Zhang, Z., and Chen, C. "Numerical study on the performance of serpentine-channel cold plates for battery thermal management". *International Journal of Heat and Mass Transfer*, (2018), 123, 536–547.

[7] Chalise, D. R., Bhattacharjee, A., and Panchal, S. "Numerical and experimental investigation of conjugate heat transfer in a liquid-cooled lithium-ion battery module". *Journal of Electrochemical Energy Conversion and Storage*, (2018), 15(1), 011008.

[8] Lagnoni, M.; Latini, D.; Nicolella, C.; Tognotti, L.; Bertei, A. "Design Guidelines for Secondary Lithium-Ion Battery Electrodes to Overcome Performance Limitations of Recycled Cathode Materials". *Journal of Energy Storage*, (2022), 50, 104237.

[9] Barbieri, M., Ceraolo, M., Lutzemberger, G., Scarpelli, C. "An Electro–Thermal Model for LFP Cells: Calibration Procedure and Validation". *Energies*, (2022), 15, 2653.

[10] Ametek Instruments. "Official Website." Available at: `https://www.ametekinstruments.it/`. Last accessed: 11 November 2025.

[11] Zentro-Elektronik. "Official Website." Available at: `https://www.zentro-elektronik.de/en/`. Last accessed: 11 November 2025.

[12] National Instruments. "Official Website." Available at: `https://www.ni.com/en.html`. Last accessed: 11 November 2025.

[13] Pasqualetto, E., Lunghi, G., Rocchio, B., Mariotti, A., and Salvetti, M. V. "Experimental characterization of the lateral and near-wake flow for the BARC configuration". *Wind and Structures*, (2022), 34(1), 101–113.

[14] Mariotti, A., Lunghi, G., Salvetti, M.V. "Experimental investigations on the effect of upstream-edge rounding on the BARC configuration". *Journal of Wind Engineering and Industrial Aerodynamics*, (2024), 251, 105787.

[15] Zwicker, M., Moghadam, M., Zhang, W., and Nielsen, C., "Automotive battery pack manufacturing – a review of battery to tab joining". *Journal of Advanced Joining Processes* , (2020), 1, 100017.